ACS NANO

Cite This: *ACS Nano* XXXX, XXX, XXX–XXX

www.acsnano.org

ARTICLE

Nanoporous Carbon: Liquid-Free Synthesis and Geometry-Dependent Catalytic Performance

Ruoyu Xu,[†] Liqun Kang,[†] Johannes Knossalla,[§] Jerrik Mielby,[‖] Qiming Wang,[†] Bolun Wang,[†] Junrun Feng,[†] Guanjie He,[⊥] Yudao Qin,[⊥] Jijia Xie,[†] Ann-Christin Swertz,[§] Qian He,[⊗] Søren Kegnæs,[‖] Dan J. L. Brett,[†] Ferdi Schüth,[§] and Feng Ryan Wang*[,†]

[†]Department of Chemical Engineering, University College London, Torrington Place, WC1E 7JE London, United Kingdom
[§]Max-Planck-Institut für Kohlenforschung, Kaiser-Wilhelm-Platz 1, 45470 Mülheim an der Ruhr, Germany
[‖]Department of Chemistry, Technical University of Denmark, 2800 Kgs. Lyngby, Denmark
[⊥]Department of Chemistry, University College London, 20 Gordon Street, Bloomsbury, WC1H 0AJ London, United Kingdom
[⊗]Cardiff Catalyst Institute, School of Chemistry, Cardiff University, CF10 3AT Cardiff, United Kingdom)

Supporting Information

ABSTRACT: **Nanostructured carbons with different pore geometries are prepared with a liquid-free nanocasting method. The method uses gases instead of liquid to disperse carbon precursors, leach templates, and remove impurities, minimizing synthetic procedures and the use of chemicals. The method is universal and demonstrated by the synthesis of 12 different porous carbons with various template sources. The effects of pore geometries in catalysis can be isolated and investigated. Two of the resulted materials with different pore geometries are studied as supports for Ru clusters in the hydrogenolysis of 5-hydroxymethylfurfural (HMF) and electrochemical hydrogen evolution (HER). The porous carbon-supported Ru catalysts outperform commercial ones in both reactions. It was found that Ru on bottleneck pore carbon shows a highest yield in hydrogenolysis of HMF to 2,5-dimethylfuran (DMF) due to a better confinement effect. A wide temperature operation window from 110 to 140 °C, with over 75% yield and 98% selectivity of DMF, has been achieved. Tubular pores enable fast charge transfer in electrochemical HER, requiring only 16 mV overpotential to reach current density of 10 mA·cm^{-2}.**

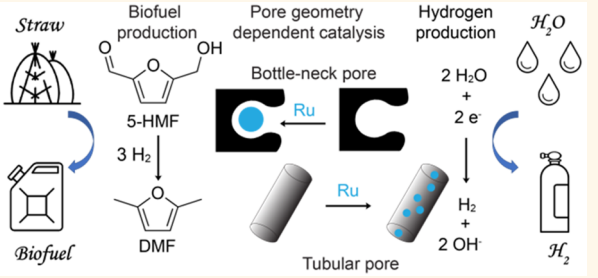

KEYWORDS: *nanoporous carbon, liquid-free synthesis, pore geometry, biomass conversion, hydrogen evolution reaction*

Substituting fossil feedstocks with renewable ones calls for efficient processes that convert biomass and green electricity to fuels and chemicals.[1,2] This requires the development of effective catalytic materials beyond the ones that are currently used for petrochemicals.[3,4] The key is to understand (i) the catalytic active-site structure, (ii) the support–active-site chemical interaction, and (iii) the local physical environment of the active site. While the former two are widely studied, the effect of local physical environment, such as pore geometry, has yet to be fully explored and optimized independently. Such an environment strongly influences the catalytic processes, determines the mass transfer efficiency, and provides confinement effects for active species.[5−7]

Nanocasting with hard templates is a well-known method to prepare porous materials. It has been applied to make porous carbon, an important class of materials widely used as supercapacitors,[8,9] effective cathode materials for lithium–sulfur batteries,[10] as well as heterogeneous catalysts.[11−16] In order to study the effects of pore geometries in these carbon materials, precise control of different pore structures *via* strictly identical synthetic procedures is needed. The synthetic steps and use of chemicals must be minimized to reduce the fluctuation of the chemical properties of the porous materials. However, these are difficult to achieve with the current nanocasting method *via* wet chemistry, which requires multistep processing, frequent solid–liquid separation, and long operation cycles.[17−20] The low efficiency of complex procedures and the unavoidable large-scale liquid waste containing environmentally unfriendly HF[21−23] or NaOH[24]

Received: December 12, 2018
Accepted: January 16, 2019
Published: January 16, 2019

DOI: 10.1021/acsnano.8b09399
ACS Nano XXXX, XXX, XXX–XXX

also limit the potential application of these carbon materials in industrial energy conversion.

In this work, we report a liquid-free synthesis of porous carbon support that leads to carbon materials with the same chemical property but different pore geometry. The synthesis follows hard-templating principles in which the creation of pores stems from an inverse replica of a porous silica template.[25−27] Uniform pore structure can therefore be achieved. Compared to the conventional method, this liquid-free synthesis uses gas for dispersing the carbon precursor, leaching templates, and removing impurities. The synthesis contains only two steps with two chemicals, which is significantly simplified compared with traditional methods. First, chemical vapor deposition (CVD) of ferrocene over a porous SiO_2 template forms a SiO_2@Fe−carbon composite. Second, porous carbon that is a direct reverse replica of the SiO_2 template is obtained by heating the composite with polytetrafluoroethylene (PTFE), in which SiO_2 is completely leached into gaseous SiF_4 (Figure 1a). The simple and liquid-free operations minimize any chemical differences of the obtained porous carbons.

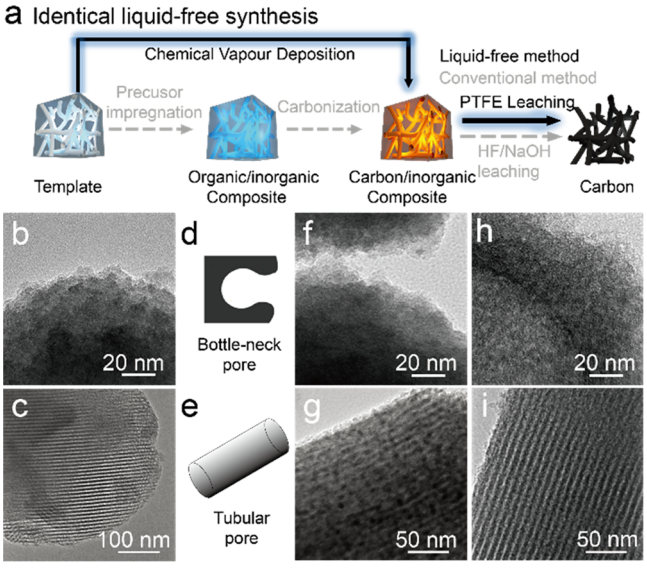

Figure 1. (a) Schematic of hard template carbon synthesis *via* liquid-free and conventional methods. (b, c) Transmission electron microscopy (TEM) images of the SiO_2@m-SiO_2 and SBA-15 templates, respectively. (d, e) Schematic of the bottleneck and tubular pores, respectively. (f, g) TEM images of the Fe/C-SiO_2@m-SiO_2 and Fe/C-SBA-15 composites, respectively. (h, i) TEM images of C-SiO_2@m-SiO_2 and C-SBA-15 composites, respectively.

Hydrogenolysis of 5-hydroxymethylfurfural (HMF) to 2,5-dimethylfuran (DMF) and electrochemical hydrogen evolution reaction (HER) are chosen for evaluating the pore geometry effect in catalysis. These two reactions involve utilizing the dissociative hydrogen atom that is one of the most essential renewable energy carriers. The effect of pore geometry plays an important role in these reactions because mass-transfer limitation and confinement effects are crucial for the transport of molecules and the dispersion of metal clusters.[16] On the basis that (1) uniform pore geometries are achieved *via* the hard template method, (2) carbon supports have the same chemical properties, and (3) as-prepared Ru clusters have same size distributions and surface oxidation states, the study of the catalytic behaviors resulting from two distinct pore geometries (bottleneck and tubular) is then possible. The Ru/C-SiO_2@m-SiO_2 catalyst with a bottleneck pore gives an outstanding catalytic performance with a yield of 90% in the hydrogenolysis of HMF to DMF. Such a high DMF yield at the moderate reaction temperature (140 °C) and low Ru/HMF molar ratio (3.5%) substantially exceeds the best reported PtCo catalysts in the literature.[11] For HER, the C-SBA-15 with tubular pores achieves the current density of 10 mA·cm^{-2} with only 16 mV overpotential, which also outperforms the commercial Pt/carbon. Bottle-neck pores, on the other hand, offer high electrochemical stability due to the confinement of active Ru species.

Finally, we demonstrate that the liquid-free synthesis is universal as it can be applied to at least 10 other types of porous carbons using five commercial zeolites (K-SSZ-13, silicate-1, Na-ZSM-5, Na-zeolite beta, and Na-zeolite Y), two commercial ordered mesoporous silica (KIT-6 and MCM-41), and three in-house made silicas (SiO_2@m-SiO_2 with half shell thickness and two mesoporous silica spheres) (Figure S1). Our scope of templates includes SSZ-13 and ZSM-5 that have a small pore size of 0.38 and 0.47 nm, respectively, significantly exceeding the pore limit of conventional wet chemistry synthesis. Such synthesis provides a library of hard templating carbon materials, enabling fundamental study on their pore geometry-dependent behaviors in catalysis, energy conversion, and storage.

RESULTS AND DISCUSSION

Ferrocene is used as the carbon source owing to its low sublimation temperature (100 °C) and high carbon-to-hydrogen ratio that provides good carbon yield.[28] The presence of Fe also catalyzes the carbonization.[29] SiO_2@m-SiO_2 and SBA-15 are used as templates to form porous carbons with bottleneck and tubular pores, respectively. The bottleneck pore origins from the use of octadecyltrimethoxysilane[30] in the ethanol−water mixture as the structure-directing agent, while that of the tubular pore stems from the use of Pluronic P123 with the presence of HCl (Figures 1b−e and S2a,b). The pore size of the SiO_2@m-SiO_2 and SBA-15 are 3.5 and 4.9 nm, respectively, while the size of the ferrocene molecule is 0.40 nm. The small ferrocene size ensures its diffusion within the pores in both systems. During the pyrolysis step, the ferrocene is oxidized to ferricenium. The strong interaction between the ferricenium and the silanol groups on the intersurface of porous silica leads to the uniformly distribution of pyrolytic carbon clusters on the pore walls of silica templates.[31] Thus, the carbon replica of SiO_2@m-SiO_2 and SBA-15 can be obtained.

During CVD, ferrocene vapor penetrates the pore systems of the templates and simultaneously decomposes into carbon and iron (Figure. 1f,g). The Fe/C-SiO_2@m-SiO_2 composite maintains the spherical morphology of the SiO_2@m-SiO_2 templates, while the tubular pore structures are still visible in the Fe/C-SBA-15 composite (Figures 1f,g and S2c,d). This indicates that ferrocene CVD does not change or affect the structure of the SiO_2 template. A comparison of N_2 physisorption before and after CVD shows the successful carbon filling of the micropore and mesopore channels in the SiO_2 templates (Figure S3). FeO_x nanoparticles are found in the composite (Figures 1f,g and S4). The presence of FeO_x nanoparticles is important as they catalyze the carbonization

DOI: 10.1021/acsnano.8b09399
ACS Nano XXXX, XXX, XXX−XXX

reaction and increase the carbon yield.[29] The oxidation state of Fe is between Fe_3O_4 and Fe_2O_3 according to X-ray absorption spectroscopy fine structure (XAFS) (Figure S5a,c) and X-ray photoelectron spectroscopy (XPS) (Figure S5e). The pore-filling degree can be calculated by the differences in pore volume (PV) before and after CVD. The filling degrees for SiO_2@m-SiO_2 and SBA-15 templates are 40% and 54%, respectively (Tables S1). The high filling degree in SBA-15 is due to the tubular channel that boosts the mass transfer during CVD.

The composites are physically mixed with PTFE powder and heated at 900 °C under N_2 in order to leach the SiO_2 (Figure S6). PTFE first decomposes into several gaseous carbon fluoride compounds which subsequently react with SiO_2, forming CO and SiF_4.[32] The overall reaction is

$$0.5n\mathrm{SiO_2} + (\mathrm{CF_2})_n \rightarrow 0.5n\mathrm{SiF_4}\uparrow + n\mathrm{CO}\uparrow$$

This reaction forms only gaseous products and leaves carbon untouched, providing instant separation of carbon during leaching. SiF_4 is then reacted with $CaCl_2$ postsynthesis, forming CaF_2 and HCl. C-SiO_2@m-SiO_2 is spherical with hollow voids originating from the solid core in SiO_2@m-SiO_2. The void diameter 180 ± 8 nm and shell thickness 40 ± 3 nm match those of the SiO_2@m-SiO_2, showing the perfect replica of the original template (Figures 1h and S2e). The ordered tubular pore structure is obtained in C-SBA15 after leaching at 900 °C, suggesting very good thermal and chemical stability (Figure. 1i). Fe nanoparticles further catalyze the carbon graphitization during PTFE leaching, as indicated in the large graphitic domain in the Raman spectroscopy of C-SiO_2@m-SiO_2 (Figure S7). In comparison, a smaller graphitic domain is obtained when Fe is removed by HCl prior to the PTFE leaching. After PTFE leaching, Fe nanoparticles cannot be found in the TEM images for both carbons (Figures 1h,i and S2e,f). The XPS and energy-dispersive X-ray spectroscopy (EDS) analysis after PTFE leaching show no obvious presence of Fe (Figures S5 and S8). The XAFS spectra indicates the initial FeO_x are reduced to metallic Fe nanoparticles in both carbons (Figure S5b,d). The Fe content is further analyzed by microwave plasma atomic emission spectroscopy (MP-AES), giving 0.97 and 0.42 wt % of Fe for C-SiO_2@m-SiO_2 and C-SBA-15, respectively (Table S2), which are much smaller than the 30 wt % Fe content in the ferrocene precursor. This indicates the separation between carbon and *in situ* formed Fe nanoparticles during the PTFE leaching at 900 °C. The thermogravimetric analysis (TGA) shows 93 and 98 wt % weight loss for C-SiO_2@m-SiO_2 and C-SBA-15 at 800 °C, respectively (Figure S9). Considering that Fe_2O_3 and SiO_2 are the major components in the TGA residue, the calculated SiO_2 contents are 5.6 and 1.4 wt % for C-SiO_2@m-SiO_2 and C-SBA-15, respectively. The porous carbons are the inverse replica of the original silica templates and have different pore geometries (Figures 2a and b). Amounts of 153 mg and 137 mg of C-SiO_2@mSiO_2 and C-SBA-15 are collected with 650 mg of ferrocene consumed. This gives the carbon yields of 23% and 21% and carbon balances of 37% and 33%, respectively, with our current lab setup. The carbon yields are close to the theoretical carbon yield of 30% that is reported in the literature using sucrose as the carbon precursor.[33] The specific surface areas for C-SiO_2@m-SiO_2 and C-SBA-15 are 806 and 872 $m^2 \cdot g^{-1}$, respectively, which are very similar to each other. The pore size and pore volume of C-SBA-15 are 4.0 nm and 0.72 $cm^3 \cdot g^{-1}$, which are higher than those of C-SiO_2@m-SiO_2 (2.2 nm and 0.56 $cm^3 \cdot g^{-1}$) (Figure 2c,d). The smaller pore size of the C-SiO_2@m-SiO_2 will have a better pore confinement effect than that of C-SBA-15. Such a pore confinement effect for metal clusters will be examined in the hydrogenolysis of 5-HMF to DMF. In addition to ferrocene, the liquid-free synthesis is suitable for a wide range of carbon precursors. C−N−SiO_2@m-SiO_2 composite (Figure S10a) and C−N−SBA-15 composite are formed during CVD using pyrrole and acetonitrile, respectively, as the carbon precursor. After PTFE leaching, the pure carbon material C−N−SBA-15 is obtained (Figure S10b).

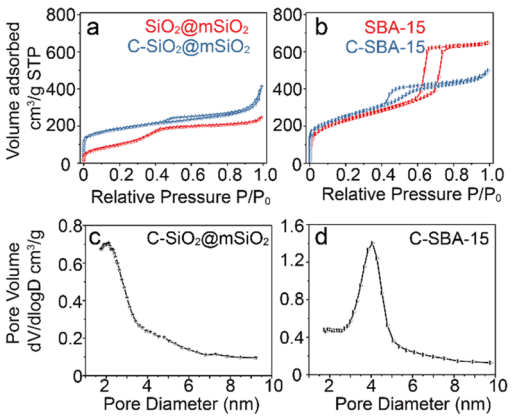

Figure 2. N_2-physisorption isotherms of (a) SiO_2@m-SiO_2 and (b) SBA-15 and their carbon replica. (c, d) Pore size distributions of C-SiO_2@m-SiO_2 and C-SBA-15, respectively.

Pore Structure−Activity Relationship in HMF Hydrogenolysis. PtCo has been identified as the benchmark for HMF to DMF conversion, suggesting an economical route to produce biofuel (DMF)[11] from a cellulose-derived platform chemical (HMF).[34] Ru is selected as a less expensive alternative to Pt and is loaded into the pore system of the porous carbon *via* wetness impregnation. Before being loaded with Ru, the C-SiO_2@m-SiO_2 and C-SBA-15 are washed with HCl solution to remove the residue of Fe and minimize any catalytic influences from those residues (Figure S11). High-angle annular dark-field scanning transmission microscopy (HAADF-STEM) reveals ultrasmall Ru clusters at 1.0 ± 0.2 and 0.9 ± 0.2 nm, evenly distributed through C-SiO_2@m-SiO_2 and C-SBA-15 support, respectively (Figure 3a,b). Such small clusters have different electronic structures and surface energy compared to that of the nanoparticles (>2 nm), leading to different catalytic behaviors.[35] Therefore, it is very important to avoid the growth of Ru clusters into nanoparticles during catalysis. The surface of Ru clusters on both carbon supports is in the oxidized form, as confirmed by the RuO_x signal in the XPS (Figures S12a,c). The carbon XPS of Ru/C-SiO_2@m-SiO_2 and Ru/C-SBA-15 also give very similar spectra. The fluorine 1s signal is found in the XPS full elements scan (Figure S11). The binding energy of the F 1s peak is between 686.5 and 687.5 eV. This is in a good agreement with the reported values of fluorinated graphite oxide (687.0 eV)[36] and different from that of PTFE (689.6 eV).[37] The Ru contents, determined by MP-AES element analysis, are 7.52 and 7.46 wt % for Ru/C-SiO_2@m-SiO_2 and Ru/C-SBA-15, respectively (Table S2). The Fe residues further reduce to 0.24 and 0.09 wt %, respectively. We, therefore conclude that initial Ru clusters in both supports are identical to each other, while the Ru−carbon interactions are also the same. The catalytic properties of

DOI: 10.1021/acsnano.8b09399
ACS Nano XXXX, XXX, XXX−XXX

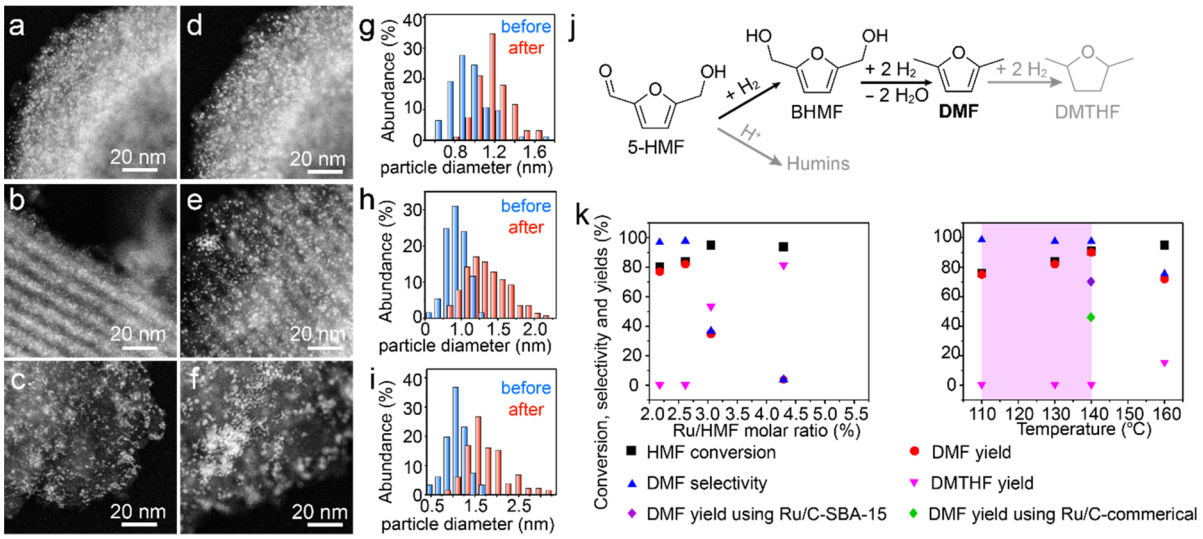

Figure 3. Hydrogenolysis of 5-HMF to DMF. (a–c) HAADF-STEM images of Ru/C-SiO$_2$@m-SiO$_2$, Ru/C-SBA-15, and Ru/C-commercial before catalysis. (d–f) HAADF-STEM images of Ru/C-SiO$_2$@m-SiO$_2$, Ru/C-SBA-15, and Ru/C-commercial after catalysis. (g–i) Histogram of Ru particle size before and after catalysis. (j) Hydrogenolysis of HMF to DMF. The main side products are DMTHF and humins. (k) Left: HMF conversion (black), DMF yield (red), DMF selectivity (blue), and DMTHF yield (pink) as a function of the Ru/HMF molar ratio. Reaction conditions: T = 130 °C; P = 10 bar H$_2$; t = 2 h; HMF 0.16 mmol in 3 mL of THF. Right: HMF conversion (black), DMF yield (red), DMF selectivity (blue), and DMTHF yield (pink) as a function of temperature. Reaction conditions: P = 10 bar H$_2$; t = 2 h; HMF 0.16 mmol in 3 mL of THF; Ru/HMF molar ratio 2.6%. The pink zone shows the 30 °C temperature window with over 75% yield of DMF and more than 98% selectivity. The DMF yields using Ru/C-SBA-15 and Ru/C-commercial are marked in purple and green, respectively.

materials with different pore geometries are then investigated independently.

The hydrogenolysis of 5-HMF comprises several steps. First, C═O is converted to C–OH, forming 2,5-hydroxymethylfuran (BHMF). C–O cleavage takes place at the two hydroxyl groups, resulting in DMF. The furan group can overreact with H$_2$, forming *cis*- and *trans*-2,5-dimethyltetrahydrofuran (DMTHF) (Figure 3j). Another route to DMF is *via* the formation of 5-methylfurfural (5-MF). HMF can also undergo polymerization to humins. A major task in this reaction is to avoid ring hydrogenation and humin formation. Ru/C-SiO$_2$@m-SiO$_2$ is studied first to obtain the best operation conditions. The molar ratio between the catalyst and 5-HMF is adjusted to maximize the DMF yield (Figure 3k, left). With a 2.2% molar ratio of Ru to HMF, 79% conversion is achieved with 77% yield and 97% selectivity to DMF at 130 °C (Figure 3k and Table S3), indicating the selective hydrogenation on the formyl group and the hydrogenolysis of the hydroxyl group at low temperature. At 2.6% molar ratio the conversion increases to 84% and the yield of DMF reaches 82%, with only a trace amount of side products. Further increase of the molar ratio to 3.1% and 4.4% causes the formation of DMTHF isomers (Figure S13), and the selectivity of DMF drops to 37% and 4%, whereas the conversion remains at 95%. Kept at a 2.6% molar ratio, the reaction temperature is then varied (Figure 3k, right). The selectivity stays above 98% from 110 to 140 °C, while the conversion increases from 76% to 91%. The drop of selectivity is observed at 160 °C, forming DMTHF. Thus, the highest yield of DMF with Ru/C-SiO$_2$@m-SiO$_2$ is 90%, achieved at 140 °C and 2.6% molar ratio. Ru/C-SBA-15 and commercial Ru/carbon (Ru/C-commercial) give 93% and 86% conversion under the same conditions, but with only 71% and 49% yields of DMF, respectively (Figure 3k, right). The low selectivity toward DMF using Ru/C-SBA-15 and commercial Ru/carbon is due to the incomplete conversion of intermediate species such as BHMF and 5-MF. The 5-HMF hydrolysis was also performed with C-SiO$_2$@mSiO$_2$, C-SBA-15, and commercial activated carbon, giving 34%, 3%, and 6% HMF conversion, respectively. The yields of DMF are only 6%, 0%, and 4% for C-SiO$_2$@m-SiO$_2$, C-SBA-15, and commercial activated carbon, respectively. The difference in HMF conversion among the three carbons comes from the slight higher Fe in the C-SiO$_2$@mSiO$_2$ than that of the others.

C-SiO$_2$@m-SiO$_2$, C-SBA-15, and C-commercial have bottleneck (2.2 nm) and tubular (4.0 nm) pores and micropores (<1 nm), respectively. The strength of the pore confinement effect to Ru clusters at 1 nm is in the order C-SiO$_2$@m-SiO$_2$ > C-SBA-15 > C-commercial (Figure 3a–c). As a result, the size of Ru clusters grows from 1.0 ± 0.2, 0.9 ± 0.2, 1.1 ± 0.5 nm to 1.2 ± 0.2, 1.5 ± 0.5, 2.0 ± 1.0 nm over C-SiO$_2$@m-SiO$_2$, C-SBA-15, C-commercial, respectively, after catalysis (Figure 3a–i). The slight increase of Ru sizes in Ru/C-SBA-15 and Ru/C-commercial during catalysis leads to the change of surface electronic structures, a decrease of the active surface, and thus the loss of activity. Cluster aggregations are found for both Ru/C-SBA-15 and Ru/C-commercial, suggesting that Ru clusters are more mobile on those supports than that of Ru/C-SiO$_2$@m-SiO$_2$ (Figures 3d–f and S14–16). The cluster aggregation on Ru/C-commercial is more severe than that on Ru/C-SBA-15, leading to a lower DMF yield of 49% than the 71% yield using the Ru/C-SBA-15 catalyst. This clearly indicates the importance of bottleneck pores in confining active Ru clusters during catalysis, showing a wide operation window from 110 to 140 °C, with over 75% yield and 98% selectivity of DMF. The temperature range of the window is the lowest compared to those reported in the literature.[38–41] Our result significantly outperforms the benchmark PtCo catalyst, which gives only 5% DMF yield at 120 °C under the same conditions and requires at least 160 °C to achieve a substantial DMF yield (Table S4).[11] These results show the superior activity of sub-nanometer Ru clusters in the hydrogenolysis of 5-HMF and,

DOI: 10.1021/acsnano.8b09399
ACS Nano XXXX, XXX, XXX–XXX

thus, the significant importance of confinement effects from the bottleneck pores that prevent the growth of the clusters.

The recycled Ru/C-SiO_2@m-SiO_2 shows 72% conversion, 68% yield, and 94% selectivity to DMF at 130 °C (Table S3, entry 9). The XPS spectrum reveals nonsignificant changes for both Ru and carbon (Figure S12b and Table S5 and S6). A slight increase of the metallic Ru crystalline domain is found in X-ray diffraction (Figure S17). This is in good agreement with X-ray absorption near-edge spectroscopy (XANES), showing the reduction of the average Ru oxidation state (Figure 4a).

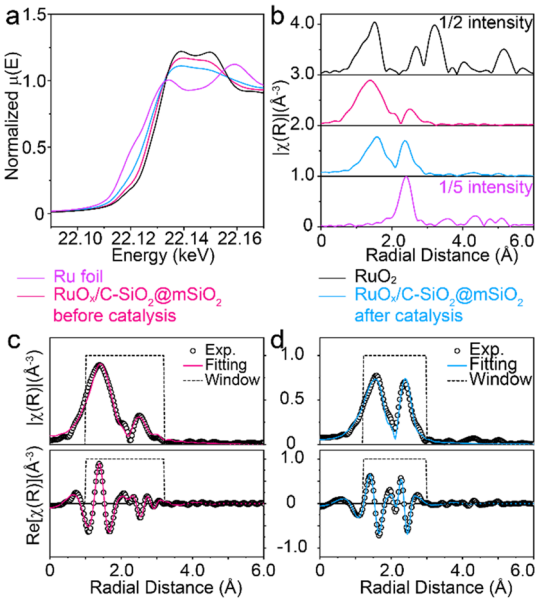

Figure 4. (a) XANES and (b) k^2-weighted R space extended X-ray absorption fine structure (EXAFS) of Ru foil (purple), Ru/C-SiO_2@m-SiO_2 before (red), after catalysis (blue), RuO_2 (black). Experimental and fitted results of Ru/C-SiO_2@m-SiO_2 in R-space EXAFS (c) before and (d) after catalysis (SBA-15), respectively.

The Ru K absorption edge position shifts to lower energy (Figure S18), and the coordination number of the first-shell Ru−Ru scattering (2.69 Å) increases from 0.7 ± 0.4 to 3.9 ± 0.8, while the Ru−O scattering coordination number decreases (Figure 4c,d and Table S7). This is due to the partial reduction of Ru by H_2 during the reaction.

Pore Structure−Activity Relationship in Electrochemical H_2 Evolution. Electrochemical HER produces CO-free H_2 for fuel cells and ammonia synthesis, where low porosity resistance[42] and efficient charge transfer[43,44] are the keys to achieving high activity. Here, the HER activities in bottleneck and tubular mesopores are studied. The same Ru clusters described above are selected as the active species due to their lower price and similar H_2 bond strength compared to that of Pt in alkaline media.[45,46] Ru/C-SBA-15 exhibits a negligible overpotential (16 mV) at a current density of 10 mA cm^{-2}, which is only one-third that of Ru/C-SiO_2@m-SiO_2 (42 mV) and commercial Pt/C (42 mV) (Figure 5a). Such low overpotential is the key indicator of high HER activity. Electrochemical impedance spectroscopy (EIS) is performed to understand their differences in porosity resistance and charge-transfer efficiency during HER reaction (Figure 5b). Here, the high-frequency semicircle (at lower Z') represents the resistance in the formation of the electrical double layer within the pore, while the low-frequency one (at higher Z')

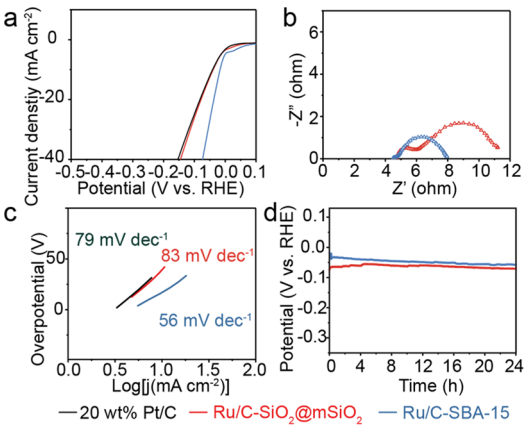

Figure 5. (a) HER polarization curves of the Ru/C-SiO_2@m-SiO_2 and Ru/C-SBA-15 compared with a commercial Pt/C catalyst in 1 M KOH. (b) EIS Nyquist plots of the of Ru/C-SiO_2@m-SiO_2 and Ru/C-SBA-15 records at −100 mV vs RHE from 100 kHz to 100 mHz. (c) Tafel plots derived from Figure 5a. (d) Time-dependent voltage curve of Ru/C-SiO_2@m-SiO_2 and Ru/C-SBA-15 under a current density of 10 mA cm^{-1} for 24 h.

corresponds to the charge-transfer resistance.[47] Thanks to the tubular pore geometry, Ru/C-SBA-15 has much smaller porosity resistance than that of bottleneck pores in Ru/C-SiO_2@m-SiO_2.[42] The charge transfer in the Ru/C-SBA-15 is also higher than that in Ru/C-SiO_2@m-SiO_2, suggesting a favored transfer mechanism in tubular pore system. We hypothesize that this is due to the diffusion of as formed H_2. The H_2 can quickly diffuse through the tubular pore and thus leave the catalytic center. In the bottom-neck pore, H_2 will be trapped inside the pore and thus block the active sites. The superior performance of the Ru/C-SBA-15 compared to that of commercial Pt/C suggests the potential of practical applications of those Ru-based catalysts in the conversion of green electricity to energy.

The fitting of the linear portions of the Tafel plots accordingly gives Tafel slopes.[48] The slopes suggest a difference in the rate-determining step for the tubular and bottleneck pores. Ru/C-SBA-15 gives a slope of 56 mV dec^{-1}, suggesting a major rate determining step following the Heyrovsky reaction ($H_2O + e^- + H^* \rightarrow H_2 + OH^-$) in the tubular pore.[45] The slope for Ru/C-SiO_2@m-SiO_2 is 83 mV dec^{-1}, indicating that in addition to the Heyrovsky reaction, the Volmer reaction ($H_2O + e^- \rightarrow H^* + OH^-$) is also the rate-determining step in the bottleneck pore (Figure 5c). The tubular pore system provides fast charge transfer of sufficient electrons for the Volmer reaction and and efficient OH^- diffusion pathway, shifting the rate-determining step to solely the Heyrovsky reaction. The stability of Ru/C-SiO_2@m-SiO_2 and Ru/C-SBA-15 catalysts are measured galvanostatically at a current density of 10 mA·cm^{-2} (Figure 5d). Within 24 h, the overpotential for Ru/C-SBA-15 increases by 39 mV, while that of Ru/C-SiO_2@m-SiO_2 only increases by 4 mV. Such a drop in stability is due to the growth and aggregation of Ru clusters in C-SBA-15 during HER. The high Ru cluster stability in HER in the bottleneck pore systems is in good agreement with that in the hydrogenolysis of 5-HMF to DMF.

Universal Liquid-Free Synthesis of Porous Carbon Materials. The catalytic behaviors of Ru/C-SiO_2@m-SiO_2 and Ru/C-SBA-15 in 5-HMF hydrogenolysis and HER clear show the important role of pore geometry in catalysis and

DOI: 10.1021/acsnano.8b09399
ACS Nano XXXX, XXX, XXX−XXX

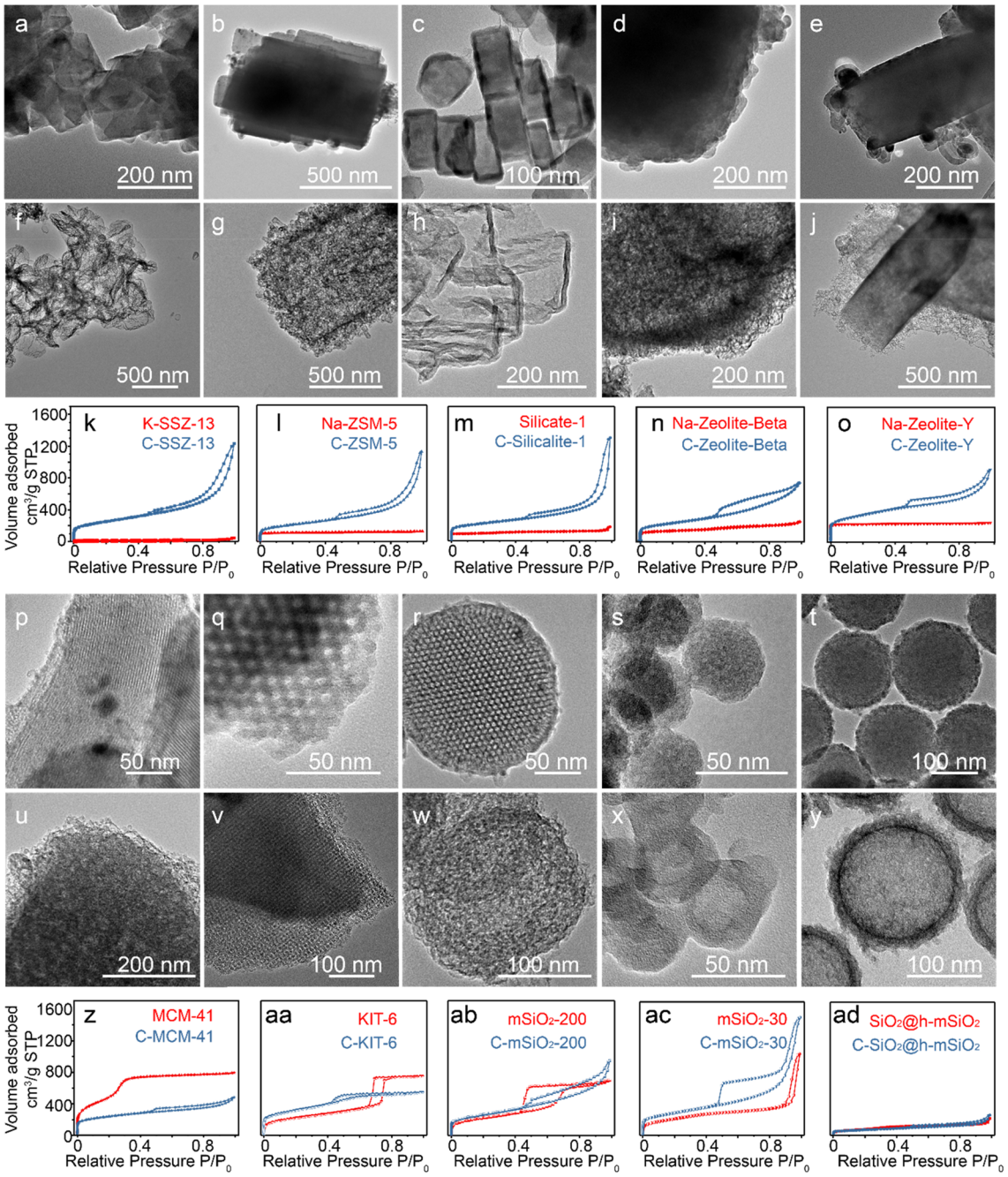

Figure 6. TEM images of 10 carbon−silica composites obtained after CVD: (a) Fe/C-SSZ-13; (b) Fe/C-ZSM-5; (c) Fe/C-silicate-1; (d) Fe/C-zeolite beta; (e) Fe/C-zeolite Y; (p) Fe/C-MCM-41; (q) Fe/C-KIT-6; (r) Fe/C-mSiO_2-200; (s) Fe/C-mSiO_2-30; and (t) Fe/C-SiO_2@mSiO_2. TEM images of 10 porous carbons obtained after PTFE leaching: (f) C-SSZ-13; (g) C-ZSM-5; (h) C-silicate-1; (i) C-zeolite beta; (j) C-zeolite Y; (u) C-MCM-41; (v) C-KIT-6; (w) C-mSiO_2-200; (x) C-mSiO_2-30; and (y) C-SiO_2@h-mSiO_2. (k−o, z−ad) Comparison of corresponding N_2 sorption between the SiO_2 templates and porous carbons. For K-SSZ-13, although the kinetic diameter of N_2 (0.36 nm) is lower than the pore aperture of SSZ-13 (3.8 Å), the low polarizability and electric quadrupole moment of N_2 result in a rather low energy of interaction when K^+ presents in the framework (Figure. 6k), showing a very low N_2 uptake.

energy conversions. Thanks to the liquid-free carbon synthesis method, a range of carbon materials with the same chemical composition but different pore geometries can be prepared. The broad application of such a method is further verified in 10 additional silica supports, which are chosen as the representative templates according to their pore size, volume, and surface area. They are K-SSZ-13, silicate-1, Na-ZSM-5, Na-zeolite beta, Na-zeolite Y, MCM-41, KIT-6, 200 nm mesoporous silica sphere (mSiO_2-200), 30 nm mesoporous silica sphere (mSiO_2-30), and SiO_2@m-SiO_2 with half-shell thickness (SiO_2@h-mSiO_2) (Figure S1). The pore sizes start from 0.38 nm for K-SSZ-13 and increase to to 5.9 nm for KIT-6 (Figure S19). The size of ferrocene is 0.33 nm between the two cyclopentadienyl groups (Cp^-) and 0.4 nm for the Cp^-. Therefore, K-SSZ-13 represents the template with the smallest pores that can be used for ferrocene CVD.

Most porous carbons keep the original morphology of the SiO_2 template (Figure 6), except for K-SSZ-13, in which the

DOI: 10.1021/acsnano.8b09399
ACS Nano XXXX, XXX, XXX−XXX

cuboid shape is slightly distorted. The diffusion of ferrocene into the zeolite framework is limited, resulting in a quasi-hollow structure where more carbons are formed at the peripheral part than at the center (Figure 6f–j). Even with silicate-1, which has the smallest particle size of 129 ± 19 nm, a clear shell with a thickness of 12 ± 3 nm is found (Figure 6h). The diffusion limitation is also found in zeolite catalysis systems, where reactions only take place within several nanometers of the zeolite surface.[49] Similar to C-SBA-15, 3D-ordered mesoporous C-KIT-6 is also obtained (Figure 6v). Unlike C-SBA-15 and C-KIT-6, the C-MCM-41 is disordered (Figure 6u), possibly due to the small pore size of MCM-41 template that leads very thin carbon walls, which are not stable at high temperature. C-mSiO_2-200, C-mSiO_2-30, and C-SiO_2@h-mSiO_2 retain the spherical morphology of the original silica template (Figure 6w–y). The diameters are 208 ± 20, 35 ± 3, and 170 ± 7 nm, respectively, corresponding well with that of the original SiO_2 templates. Trace amounts of Fe and Al are found in the C-Na-zeolite-Y, giving 0.30 and 1.54 wt % from MP-AES analysis, respectively (Table S2). All porous carbons are the inverse replica of the original silica templates and have different pore geometries (Figure 6). Hysteresis between 0.4 and 0.9 P/P_0 is found for all five zeolite-templated carbons, showing the formation of mesopores inside the carbon cuboid. The mesopores are also found in all mesopore silica templated carbons. The well-controlled synthesis of carbon materials with different pore structures enables a fundamental understanding of pore geometry effects in chemical reactions.

CONCLUSIONS

Ru clusters in bottleneck and tubular carbon pores are studied in the 5-HMF hydrogenolysis and HER. Bottleneck pores successfully confine the Ru clusters size around 1 nm during catalysis, showing twice the DMF yield of unconfined clusters and better stability in HER. The tubular pore has low porosity resistance and provides efficient charge transfer in HER, requiring only 16 mV overpotential to reach current density of 10 mA·cm^{-2}. The difference in catalytic activity is mainly pore geometry dependent, while the chemical properties of Ru clusters and carbon support are kept the same. The fast and liquid-free synthesis of carbon support with different pore geometry is general applicable, with 10 additional syntheses of porous carbon templated from commercial zeolite and mesoporous silica. The use of gas for dispersing chemicals, leaching templates, and removing impurities is advantageous in the material innovations that are important for catalysis, energy conversion, and storage applications.

EXPERIMENTAL METHODS

Synthesis of SiO_2@m-SiO_2 and SiO_2@h-mSiO_2 Templates. To obtain a solid SiO_2 core, ethanol (552.3 g), H_2O (132.53 mL), NH_3 (28–30%, 12.83 mL) and tetraethyl orthosilicate (TEOS, 27.77 mL) were mixed in a 1000 mL round-bottom flask. The mixture was stirred for 12 h at room temperature. To synthesize the mesoporous SiO_2 shell, TEOS (19.72 mL) and octadecyltrimethoxysilane (OTMS, 7.78 mL) were then added to the aforementioned mixture. The mixture was then stirred for another 12 h. Half amounts of TEOS (9.86 mL) and OTMS (3.89 mL) were used to synthesize the half-shell template. The product was collected by centrifugation and placed in an oven to dry. Approximately, 8.5 g of white product was obtained in each batch. The sample was calcined at 550 °C for 1.5 h with a heating rate of 1.5 °C min^{-1} for the removal of the alkyl chains contained in OTMS.

Synthesis of mSiO_2-30. A 7.675 g portion of ethyltrimethylammonium bromide (CTAB) was dissolved in 500 mL of deionized water in a polypropylene bottle. The suspension was stirred for 5 min and subsequently sonicated for 20 min. Afterward, the solution was placed in an oven at 100 °C for 10 min. Then 1.545 mL of triethanolamine was added, and the solution was stirred at 80 °C for 1 h. Then 77.55 mL of TEOS was rapidly added to the stirring solution, which was subsequently stirred at 80 °C for 2 h. The product was collected by centrifugation and placed in an oven to dry. The sample was calcined at 550 °C for 1.5 h with a heating rate of 1.5 °C min^{-1} for the removal of the alkyl chains contained in CTAB and TEOS.

Synthesis of mSiO_2-200. A 0.8 g portion of CTAB and 4.8 mL of 30% ammonia–water were dissolved in 118 mL of deionized water in a 500 mL round-bottom flask. The suspension was stirred for 5 min. The mixture of TOES (4 mL) and hexane (16 mL) was added into the solution dropwise, and the solution was stirred for 12 h. The product was collected by centrifugation and placed in an oven to dry. The sample was calcined at 550 °C for 1.5 h with a heating rate of 1.5 °C min^{-1} for the removal of the alkyl chains contained in CTAB and TEOS.

Synthesis of Porous Carbon Materials *via* Various Templates. The porous carbon materials were prepared by using the CVD method with different zeolites and SiO_2 as the templates and ferrocene as the carbon source. Ferrocene (2 g) and zeolite/SiO_2 (500 mg) were placed in different heating zones within the two-stage tubular furnace. The sublimation and the pyrolysis of the ferrocene were conducted in 56 mL min^{-1} argon flow at 120 and 550 °C, respectively, for 2 h. The weight loss for ferrocene during CVD is 650 mg. The as-prepared Fe-carbon@SiO_2 composite (500 mg) was mixed with PTFE (4 g) and heated under 1 L min^{-1} nitrogen flow at 900 °C for 4 h to subsequently leach silica.

Synthesis of Ru/C-SiO_2@m-SiO_2 and Ru/C-SBA-15. Before loading of Ru, the carbon material, C-SiO_2@m-SiO_2, was washed with HCl solution. $RuCl_3$ (Ru 38%, 137 mg, 0.52 mmol) was dissolved in water (0.22 mL) and then impregnated into the C-SiO_2@m-SiO_2 powder (470 mg) under stirring until it was mixed uniformly and then dried at 60 °C. The mixture was heated at 220 °C under 15% hydrogen/argon for 3 h. The same method was used to prepared Ru/C-SBA-15

Hydrogenolysis of 5-Hydroxymethylfurfural. For a typical experiment, HMF (20 mg, 0.16 mmol), tetrahydrofuran (THF, 3 mL), dodecane (1.37 mg, 0.008 mmol), and different amounts of catalyst were added into a Teflon inset, transferred into a stainless-steel autoclave reactor, and then sealed and purged with hydrogen three times. The reaction was performed at the target temperature with 10 bar of initial hydrogen pressure under 400 rpm stirring. After the desired reaction time, the reactor was cooled to room temperature. The solution was filtered and analyzed by gas chromatography–mass spectrometry (GC–MS). The catalysts were collected by centrifugation, washed with THF several times, and then reduced by hydrogen again before recycling.

Electrochemical Measurement. All of the tests were carried out using an Autolab (Metrohm PGSTAT302N) electrochemical station by a three-electrode method with a glassy carbon rotating disk as the working electrode and carbon rod and Ag/AgCl/saturated KCl as counter and reference electrode in alkaline electrolyte (1 M KOH) at room temperature. All of the measurements were carried out with a fixed catalyst deposition of ~0.28 mg cm^{-2} on a 3 mm in diameter (or area of 0.0707 cm^2) glassy carbon disk electrode. The catalyst was prepared as follows: 2 mg of sample was dispersed in a total of 540 μL of solution consisting 500 μL of 4:1 v/v water/ethanol and 40 μL of Nafion (5% solution) under sonication. The sonication was carried out up to 1 h to obtain uniform catalyst dispersion ink, of which 5 μL was micropipetted and dropped on to a GCDE followed by drying at 60 °C in the oven prior to the electrochemical tests. All of the electrochemical test results were reported with respect to the reference, Ag/AgCl. The HER liner sweep voltammetry (LSV) curves were measured at disk rotating speeds of 1600 rpm. Stability tests were carried under a current of 0.707 mA for 24 h. EIS was taken from 100k Hz to 100m Hz at −100 mV vs RHE.

DOI: 10.1021/acsnano.8b09399
ACS Nano XXXX, XXX, XXX–XXX

Characterization. TEM was performed using a JEOL JEM-2100 microscope equipped with an Oxford Instruments EDS detector at 200 kV. Particle size distributions were estimated through measurement of 100 particles. Scanning electron microscopy (SEM) imaging was performed on a JEOL JSM-7401F SEM. Scanning transmission electron microscopy (STEM) was performed using a probe corrected (CEOS) JEM ARM 200CF (JEOL, Japan) equipped with detectors for bright-field (BF), high-angle annular dark-field (HAADF) and secondary electron (SE) imaging at 200 kV. X-ray diffraction (XRD) measurements were performed using a StadiP diffractometer from STOE, a voltage of 40 kV, at 30 mA, with a Cu source with $K_{\alpha 1}$ = 1.540562 Å and $K_{\alpha 2}$ = 1.544398 Å. The signal from $K_{\alpha 2}$ was removed for analysis. XPS) analyses were performed on a Thermoscientific XPS K-α surface analysis machine using an Al source. Analysis was performed on the Casa XPS software. Elemental analysis was performed using an Agilent 4100 microwave plasma-atomic emission spectrometer. Solid samples were digested in aqua regia. Each sample was measured three times to ensure reliable results. The results show the average of the measurements recorded. Thermogravimetric analysis was carried by PerkinElmer Pyris 1 TGA in nitrogen flow from 30 to 900 °C. Nitrogen adsorption−desorption isotherms were recorded at 77 K using a Micromeritics 3Flex surface characterization analyzer. The samples were degassed at 300 °C overnight. Specific surface areas were determined according to the BET model, with pore diameters, volumes, and distributions determined through the BJH method. X-ray absorption near-edge structure (XANES) and extended X-ray absorption fine structure (EXAFS) analysis of the Ru K edge (22.117 keV) and the Fe K edge (7.112 keV) were carried out at 3.0 GeV with a beam current of 300 mA on the Beamline B18 of the Diamond Light Source (UK). Samples were diluted by cellulose and pressed into a 0.8 cm diameter pellets for measurement.). Ru foil, RuO_2, Fe foil, FeO (wüstite), Fe_2O_3 (hematite), and Fe_3O_4 (magnetite) were measured as the standard for energy shift calibration. The XAFS spectra of all samples were measured in transmission mode in an energy range of 21.9−23.2 keV for Ru K edge and 6.91 to 7.66 keV for Fe K edge with a beam size of 200 μm (H) × 250 μm (V). The spectrum of each sample was measured five times and merged to improve the signal-to-noise ratio. Athena software was used for data extraction and XANES analysis. Artemis software was used to fit the k^2-weighted EXAFS data in real space with 3.4 Å^{-1} < k < 13.5 Å^{-1} and 1.0 Å < R < 3.0 Å.[50,51] Raman spectra were recorded on a Renishaw InVia Raman spectrometer in a backscattered confocal configuration using 647 nm laser excitation.

ASSOCIATED CONTENT

Supporting Information

The Supporting Information is available free of charge on the ACS Publications website at DOI: 10.1021/acsnano.8b09399.

TEM and SEM images, N_2-physisorption isotherms, XPS spectra, Raman spectra, XAFS spectra and fittings, XRD patterns, and catalytic results (Figures S1−S19 and Tables S1−S7) (PDF)

AUTHOR INFORMATION

Corresponding Author

*E-mail: ryan.wang@ucl.ac.uk.

ORCID

Liqun Kang: 0000-0003-2100-4310
Johannes Knossalla: 0000-0002-2220-6670
Jerrik Mielby: 0000-0001-6588-2495
Yudao Qin: 0000-0002-3623-2319
Jijia Xie: 0000-0003-4609-8915
Søren Kegnæs: 0000-0002-6933-6931
Feng Ryan Wang: 0000-0002-2475-606X

Author Contributions

F.R.W. and R.X. conceived the presented idea and wrote the manuscript with support from B.W., F.S., and D.J.L.B. R.X planned and carried out the synthesis and experiments. L.K. contributed to the X-ray absorption near-edge spectroscopy analysis. Q.W., J.K., J.M., S.K, J.F., and J.X. contributed to sample preparation and analysis. G.H. and Y.Q contributed to the electrochemical measurements. A.-C.S. and Q.H. contributed to the transmission electron microscopy measurements. All authors provided critical feedback and helped shape the research, analysis, and manuscript.

Notes

The authors declare no competing financial interest.

ACKNOWLEDGMENTS

This work was conducted with the support from EPSRC First Grant project (EP/P02467X/1, EP/S018204/1), Royal Society research grant (RG160661), and Royal Society International Exchange (IES\R3\170097). We acknowledge Diamond Light Source and the UK Catalysis Hub block allocation for beamtime (SP15151, SP206191), the rapid access beamtime (EM21370), the B18 and E01 beamline scientists Diego Gianolio, Giannantonio Cibin, and Mohsen Danaie for their help. The UK Catalysis Hub is kindly thanked for resources and support provided *via* our membership in the UK Catalysis Hub Consortium and funded by EPSRC (portfolio grants EP/K014706/1, EP/K014668/1, EP/K014854/1, EP/K014714/1, and EP/I019693/1). We are grateful for the funding provided by the Max-Planck-Institut für Kohlenforschung, the Cluster of Excellence TMFB, and the Danish Council for Independent Research (Grant No. 5054-00119). R.X thanks the China Scholarship Council (CSC) for the Ph.D. funding. B.W. thanks the Newton International Fellowship (NF170761) for funding support.

REFERENCES

(1) Roman-Leshkov, Y.; Barrett, C. J.; Liu, Z. Y.; Dumesic, J. A. Production of Dimethylfuran for Liquid Fuels from Biomass-Derived Carbohydrates. *Nature* **2007**, *447*, 982−985.
(2) Greeley, J.; Markovic, N. M. The Road from Animal Electricity to Green Energy: Combining Experiment and Theory in Electrocatalysis. *Energy Environ. Sci.* **2012**, *5*, 9246−9256.
(3) Jiao, Y.; Zheng, Y.; Jaroniec, M. T.; Qiao, S. Z. Design of Electrocatalysts for Oxygen- and Hydrogen-Involving Energy Conversion Reactions. *Chem. Soc. Rev.* **2015**, *44*, 2060−2086.
(4) Seh, Z. W.; Kibsgaard, J.; Dickens, C. F.; Chorkendorff, I. B.; Norskov, J. K.; Jaramillo, T. F. Combining Theory and Experiment in Electrocatalysis: Insights into Materials Design. *Science* **2017**, *355*, No. eaad4998.
(5) Tang, K.; Fu, L. J.; White, R. J.; Yu, L. H.; Titirici, M. M.; Antonietti, M.; Maier, J. Hollow Carbon Nanospheres with Superior Rate Capability for Sodium-Based Batteries. *Adv. Energy Mater.* **2012**, *2*, 873−877.
(6) Su, D. S.; Perathoner, S.; Centi, G. Nanocarbons for the Development of Advanced Catalysts. *Chem. Rev.* **2013**, *113*, 5782−5816.
(7) Zhu, J.; Holmen, A.; Chen, D. Carbon Nanomaterials in Catalysis: Proton Affinity, Chemical and Electronic Properties, and their Catalytic Consequences. *ChemCatChem* **2013**, *5*, 378−401.
(8) Zhang, L. L.; Zhao, X. S. Carbon-based Materials as Supercapacitor Electrodes. *Chem. Soc. Rev.* **2009**, *38*, 2520−2531.
(9) Simon, P.; Gogotsi, Y. Materials for Electrochemical Capacitors. *Nat. Mater.* **2008**, *7*, 845−854.

DOI: 10.1021/acsnano.8b09399
ACS Nano XXXX, XXX, XXX−XXX

(10) Ji, X. L.; Lee, K. T.; Nazar, L. F. A Highly Ordered Nanostructured Carbon-Sulphur Cathode for Lithium-Sulphur Batteries. *Nat. Mater.* **2009**, *8*, 500−506.
(11) Wang, G. H.; Hilgert, J.; Richter, F. H.; Wang, F.; Bongard, H. J.; Spliethoff, B.; Weidenthaler, C.; Schuth, F. Platinum-Cobalt Bimetallic Nanoparticles in Hollow Carbon Nanospheres for Hydrogenolysis of 5-Hydroxymethylfurfural. *Nat. Mater.* **2014**, *13*, 293−300.
(12) Arnal, P. M.; Comotti, M.; Schuth, F. High-Temperature-Stable Catalysts by Hollow Sphere Encapsulation. *Angew. Chem., Int. Ed.* **2006**, *45*, 8224−8227.
(13) Baldizzone, C.; Mezzavilla, S.; Carvalho, H. W. P.; Meier, J. C.; Schuppert, A. K.; Heggen, M.; Galeano, C.; Grunwaldt, J. D.; Schuth, F.; Mayrhofer, K. J. J. Confined-Space Alloying of Nanoparticles for the Synthesis of Efficient PtNi Fuel-Cell Catalysts. *Angew. Chem., Int. Ed.* **2014**, *53*, 14250−14254.
(14) Ortac, I.; Simberg, D.; Yeh, Y.-s.; Yang, J.; Messmer, B.; Trogler, W. C.; Tsien, R. Y.; Esener, S. Dual-Porosity Hollow Nanoparticles for the Immunoprotection and Delivery of Nonhuman Enzymes. *Nano Lett.* **2014**, *14*, 3023−3032.
(15) Lee, J.; Kim, S. M.; Lee, I. S. Functionalization of Hollow Nanoparticles for Nanoreactor Applications. *Nano Today* **2014**, *9*, 631−667.
(16) Prieto, G.; Tuysuz, H.; Duyckaerts, N.; Knossalla, J.; Wang, G. H.; Schuth, F. Hollow Nano- and Microstructures as Catalysts. *Chem. Rev.* **2016**, *116*, 14056−14119.
(17) Wu, S. H.; Tseng, C. T.; Lin, Y. S.; Lin, C. H.; Hung, Y.; Mou, C. Y. Catalytic Nano-Rattle of Au@Hollow Silica: Towards a Poison-Resistant Nanocatalyst. *J. Mater. Chem.* **2011**, *21*, 789−794.
(18) Li, Y. Q.; Bastakoti, B. P.; Imura, M.; Tang, J.; Aldalbahi, A.; Torad, N. L.; Yamauchi, Y. Dual Soft-Template System Based on Colloidal Chemistry for the Synthesis of Hollow Mesoporous Silica Nanoparticles. *Chem. - Eur. J.* **2015**, *21*, 6375−6380.
(19) Lim, J.; Um, J. H.; Ahn, J.; Yu, S. H.; Sung, Y. E.; Lee, J. K. Soft Template Strategy to Synthesize Iron Oxide-Titania Yolk-Shell Nanoparticles as High-Performance Anode Materials for Lithium-Ion Battery Applications. *Chem. - Eur. J.* **2015**, *21*, 7954−7961.
(20) Deng, X. H.; Chen, K.; Tuysuz, H. Protocol for the Nanocasting Method: Preparation of Ordered Mesoporous Metal Oxides. *Chem. Mater.* **2017**, *29*, 40−52.
(21) Bottger-Hiller, F.; Kempe, P.; Cox, G.; Panchenko, A.; Janssen, N.; Petzold, A.; Thurn-Albrecht, T.; Borchardt, L.; Rose, M.; Kaskel, S.; Georgi, C.; Lang, H.; Spange, S. Twin Polymerization at Spherical Hard Templates: an Approach to Size-Adjustable Carbon Hollow Spheres with Micro- or Mesoporous Shells. *Angew. Chem., Int. Ed.* **2013**, *52*, 6088−6091.
(22) Yoon, S. B.; Sohn, K.; Kim, J. Y.; Shin, C. H.; Yu, J. S.; Hyeon, T. Fabrication of Carbon Capsules with Hollow Macroporous Core/Mesoporous Shell Structures. *Adv. Mater.* **2002**, *14*, 19−21.
(23) Valle-Vigon, P.; Sevilla, M.; Fuertes, A. B. Synthesis of Uniform Mesoporous Carbon Capsules by Carbonization of Organosilica Nanospheres. *Chem. Mater.* **2010**, *22*, 2526−2533.
(24) Li, J. J.; Liang, Y.; Dou, B. J.; Ma, C. Y.; Lu, R. J.; Hao, Z. P.; Xie, Q.; Luan, Z. Q.; Li, K. Nanocasting Synthesis of Graphitized Ordered Mesoporous Carbon Using Fe-Coated SBA-15 Template. *Mater. Chem. Phys.* **2013**, *138*, 484−489.
(25) Lu, A. H.; Schüth, F. Nanocasting: a Versatile Strategy for Creating Nanostructured Porous Materials. *Adv. Mater.* **2006**, *18*, 1793−1805.
(26) Lou, X. W. D.; Archer, L. A.; Yang, Z. Hollow Micro-/Nanostructures: Synthesis and Applications. *Adv. Mater.* **2008**, *20*, 3987−4019.
(27) Xia, Y.; Mokaya, R. Hollow Spheres of Crystalline Porous Metal Oxides: A Generalized Synthesis Route *via* Nanocasting with Mesoporous Carbon Hollow Shells. *J. Mater. Chem.* **2005**, *15*, 3126−3131.
(28) Andrews, R.; Jacques, D.; Rao, A. M.; Derbyshire, F.; Qian, D.; Fan, X.; Dickey, E. C.; Chen, J. Continuous Production of Aligned Carbon Nanotubes: a Step Closer to Commercial Realization. *Chem. Phys. Lett.* **1999**, *303*, 467−474.
(29) Sevilla, M.; Sanchis, C.; Valdes-Solis, T.; Morallon, E.; Fuertes, A. B. Synthesis of Graphitic Carbon Nanostructures from Sawdust and Their Application as Electrocatalyst Supports. *J. Phys. Chem. C* **2007**, *111*, 9749−9756.
(30) Galeano, C.; Meier, J. C.; Peinecke, V.; Bongard, H.; Katsounaros, I.; Topalov, A. A.; Lu, A. H.; Mayrhofer, K. J. J.; Schuth, F. Toward Highly Stable Electrocatalysts *via* Nanoparticle Pore Confinement. *J. Am. Chem. Soc.* **2012**, *134*, 20457−20465.
(31) Schnitzler, M. C.; Mangrich, A. S.; Macedo, W. A. A.; Ardisson, J. D.; Zarbin, A. J. G. Incorporation, Oxidation and Pyrolysis of Ferrocene into Porous Silica Glass: a Route to Different Silica/Carbon and Silica/Iron Oxide Nanocomposites. *Inorg. Chem.* **2006**, *45*, 10642−10650.
(32) Singh, D. K.; Krishna, K. S.; Harish, S.; Sampath, S.; Eswaramoorthy, M. No More HF: Teflon-Assisted Ultrafast Removal of Silica to Generate High-Surface-Area Mesostructured Carbon for Enhanced CO_2 Capture and Supercapacitor Performance. *Angew. Chem., Int. Ed.* **2016**, *55*, 2032−2036.
(33) Shin, H. J.; Ryoo, R.; Kruk, M.; Jaroniec, M. Modification of SBA-15 Pore Connectivity by High-Temperature Calcination Investigated by Carbon Inverse Replication. *Chem. Commun.* **2001**, 349−350.
(34) Artz, J.; Mallmann, S.; Palkovits, R. Selective Aerobic Oxidation of HMF to 2,5-Diformylfuran on Covalent Triazine Frameworks-Supported Ru Catalysts. *ChemSusChem* **2015**, *8*, 672−679.
(35) Zhang, H. B.; Liu, G. G.; Shi, L.; Ye, J. H. Single-Atom Catalysts: Emerging Multifunctional Materials in Heterogeneous Catalysis. *Adv. Energy Mater.* **2018**, *8*, 1701343.
(36) Jankovsky, O.; Simek, P.; Sedmidubsky, D.; Matejkova, S.; Janousek, Z.; Sembera, F.; Pumera, M.; Sofer, Z. Water-Soluble Highly Fluorinated Graphite Oxide. *RSC Adv.* **2014**, *4*, 1378−1387.
(37) Girardeaux, C.; Pireaux, J.-J. Analysis of Poly-(tetrafluoroethylene) (PTFE) by XPS. *Surf. Sci. Spectra* **1996**, *4*, 138−141.
(38) Zhu, Y. F.; Kong, X.; Zheng, H. Y.; Ding, G. Q.; Zhu, Y. L.; Li, Y. W. Efficient Synthesis of 2,5-Dihydroxymethylfuran and 2,5-Dimethylfuran from 5-Hydroxymethylfurfural Using Mineral-Derived Cu Catalysts as Versatile Catalysts. *Catal. Sci. Technol.* **2015**, *5*, 4208−4217.
(39) Hu, L.; Tang, X.; Xu, J. X.; Wu, Z.; Lin, L.; Liu, S. J. Selective Transformation of 5-Hydroxymethylfurfural into the Liquid Fuel 2,5-Dimethylfuran over Carbon-Supported Ruthenium. *Ind. Eng. Chem. Res.* **2014**, *53*, 3056−3064.
(40) Zu, Y. H.; Yang, P. P.; Wang, J. J.; Liu, X. H.; Ren, J. W.; Lu, G. Z.; Wang, Y. Q. Efficient Production of the Liquid Fuel 2,5-Dimethylfuran from 5-Hydroxymethylfurfural over Ru/Co_3O_4 Catalyst. *Appl. Catal., B* **2014**, *146*, 244−248.
(41) Saha, B.; Bohn, C. M.; Abu-Omar, M. M. Zinc-Assisted Hydrodeoxygenation of Biomass-Derived 5-Hydroxymethylfurfural to 2,5-Dimethylfuran. *ChemSusChem* **2014**, *7*, 3095−3101.
(42) Chen, Z. X.; Leng, K.; Zhao, X. X.; Malkhandi, S.; Tang, W.; Tian, B. B.; Dong, L.; Zheng, L. R.; Lin, M.; Yeo, B. S.; Loh, K. P. Interface Confined Hydrogen Evolution Reaction in Zero Valent Metal Nanoparticles-Intercalated Molybdenum Disulfide. *Nat. Commun.* **2017**, *8*, 14548.
(43) Wang, L.; Xia, M.; Wang, H.; Huang, K.; Qian, C.; Maravelias, C. T.; Ozin, G. A. Greening Ammonia toward the Solar Ammonia Refinery. *Joule* **2018**, *2*, 1055−1074.
(44) Turner, J. A. Sustainable Hydrogen Production. *Science* **2004**, *305*, 972−974.
(45) Wang, J.; Wei, Z. Z.; Mao, S. J.; Li, H. R.; Wang, Y. Highly Uniform Ru Nanoparticles over N-doped Carbon: pH and Temperature-Universal Hydrogen Release from Water Reduction. *Energy Environ. Sci.* **2018**, *11*, 800−806.
(46) Xu, J.; Liu, T.; Li, J.; Li, B.; Liu, Y.; Zhang, B.; Xiong, D.; Amorim, I.; Li, W.; Liu, L. Boosting the Hydrogen Evolution

DOI: 10.1021/acsnano.8b09399
ACS Nano XXXX, XXX, XXX−XXX

Performance of Ruthenium Clusters Through Synergistic Coupling with Cobalt Phosphide. *Energy Environ. Sci.* **2018**, *11*, 1819−1827.
(47) Hitz, C.; Lasia, A. Experimental Study and Modeling of Impedance of the HER on Porous Ni Electrodes. *J. Electroanal. Chem.* **2001**, *500*, 213−222.
(48) Yang, Y.; Fei, H. L.; Ruan, G. D.; Tour, J. M. Porous Cobalt-Based Thin Film as a Bifunctional Catalyst for Hydrogen Generation and Oxygen Generation. *Adv. Mater.* **2015**, *27*, 3175−3180.
(49) Meirer, F.; Kalirai, S.; Morris, D.; Soparawalla, S.; Liu, Y. J.; Mesu, G.; Andrews, J. C.; Weckhuysen, B. M. Life and Death of a Single Catalytic Cracking Particle. *Science Advances* **2015**, *1*, No. e1400199.
(50) Dent, A.; Cibin, G.; Ramos, S.; Parry, S.; Gianolio, D.; Smith, A.; Scott, S.; Varandas, L.; Patel, S.; Pearson, M. In Performance of B18, the Core EXAFS Bending Magnet Beamline at Diamond. *J. Phys.: Conf. Ser.* **2013**, *430*, 012023.
(51) Dent, A.; Cibin, G.; Ramos, S.; Smith, A.; Scott, S.; Varandas, L.; Pearson, M.; Krumpa, N.; Jones, C.; Robbins, P. In B18: A Core XAS Spectroscopy Beamline for Diamond. *J.Phys.: Conf. Ser.* **2009**, *190*, 012039.

DOI: 10.1021/acsnano.8b09399
ACS Nano XXXX, XXX, XXX−XXX